

Effect of Cooling Process on Microstructure and Properties of Low Carbon Bainite Steel

Zhifeng CAO¹, JiMan WANG¹, Shenggang ZHOU^{2*}, Hu YAN²

¹ Dongying Institute of Special Equipment Inspection, Dongying, Shandong 257200, China

² School of Materials Science and Engineering, KunMing University of Technology, KunMing, Yunnan 650093, China

<http://doi.org/10.5755/j02.ms.34199>

Received 25 May 2023; accepted 30 August 2023

This article used Mn-Mo-Cr-B low-carbon bainitic steel as the experimental material. The continuous cooling transformation curve of the steel during continuous cooling was determined using a Gleeble-1500D thermal simulation test machine, and a corresponding phase transformation model for bainitic steel during continuous cooling was established. The influence of different cooling rates and final cooling temperatures on the microstructure and mechanical properties of the steel was investigated. Employing metallography, SEM, and EBSD techniques, the microstructure, crystallographic orientation, and grain boundary angle distribution of the low-carbon bainitic steel were explored, and their relationship with the steel's strength and toughness was studied. The research findings reveal that varying cooling rates and final cooling temperatures impact the phase transformation process and microstructure of the steel, consequently affecting its mechanical properties indirectly. With increasing cooling rate, the diffusion and fineness of martensite increase, and the quantity of lath bainite grows while the laths become finer. Elevated final cooling temperatures lead to larger martensitic-austenitic (MA) islands and reduced lath bainite quantity, causing the laths to become wider. Through analysis of the substructure of bainitic steel, it was determined that the bainite organization in the tested steel comprises primary austenite grains, lath packet, and lath block in succession. Lath packets are composed of lath blocks with different orientations, where lath size predominantly controls strength. Finer lath size corresponds to higher strength, and the influence of substructure on toughness is comparatively minor.

Keywords: low carbon bainitic steel, cooling process, thermal simulation, crystallographic orientation, lath block, laths packet.

1. INTRODUCTION

Low carbon bainitic steel is a new type of high-strength, high-toughness, versatile and weldable steel that has been developed internationally in the last 30 years, and is referred to as the steel of the 21st century [1, 2]. The steel utilizes modern steelmaking methods, such as ladle refining and continuous casting, to obtain highly distorted austenite grains in the high-temperature non-crystalline zone by controlled rolling. By adding elements that improve hardenability (Mn, Cu, Mo, B) to the steel and controlling the cooling conditions after rolling, the deformed austenite is transformed into a variety of fine bainite structures, which greatly increases the yield strength of the steel [3–6]. The reduced carbon content of this type of steel eliminates the adverse effects of carbon on the bainite structure's toughness [7–9]. It is widely used in many fields such as oil and gas pipelines, engineering machinery, pressure vessels, containers, bridges, and ships.

The bainitic structure of low carbon bainitic steel is diverse and is composed of a mixed structure of several non-equilibrium structures, including quasi-polygonal ferrite, needle-shaped ferrite, granular bainite, lath bainite, and martensite-austenite (MA) islands [10–13]. The steel's properties depend on its microstructure, which is mainly determined by phase transformation. Under the same steel composition and production process, cooling conditions

have a significant impact on the phase transformation process. Due to its high strength and good toughness, low carbon bainitic steel has attracted more and more researchers' exploration [14–16]. The cooling process in the steel's production affects the temperature gradient, resulting in uneven stress and performance differences [17, 18]. Therefore, reasonable optimization of the cooling process can not only optimize product performance but also contribute to energy conservation and emission reduction [19].

This study utilized Mn-Mo-Cr-B low-carbon bainitic steel produced by Anyang Iron and Steel as the experimental material. Due to constraints in the production process, this steel was not subjected to tempering, resulting in an unstable mechanical performance. While achieving the desired strength level seemed attainable, its ductility was limited, and the impact toughness values were inconsistent. To investigate the possible reasons behind this performance paradox and to identify potential solutions, this research commenced with an examination of the microstructure of the low-carbon bainitic steel. Thermal simulation tests were employed to explore its phase transformation characteristics. By adjusting cooling rates and final cooling temperatures, the continuous cooling transformation (CCT) curve of the tested steel during continuous cooling was successfully determined, and a phase transformation model for bainitic steel during continuous cooling was established.

* Corresponding author. Tel.: +86-13888318583.
E-mail: zsgandy@kust.edu.cn (S. Zhou)

Furthermore, utilizing experimental instruments such as scanning electron microscopy (SEM), electron backscatter diffraction (EBSD), and transmission electron microscopy (TEM), a comprehensive analysis was conducted on the impact of cooling processes during the production of low-carbon bainitic steel on its microstructural features, grain orientation, and grain boundary angle distribution. Additionally, an in-depth investigation was carried out to discern the relationship between microstructural features and their substructures and the material's strength and toughness. The primary aim of this study is to unveil the governing principles of how cooling processes influence the microstructure and performance of the product. By delving into the understanding of performance contradictions, microstructural characteristics, and the impact of process parameters on performance, we anticipate discovering methods to enhance the performance of this series of steel while also reducing production costs. This endeavour holds significant value in terms of guidance and practicality for engineering applications.

2. EXPERIMENTAL MATERIALS AND METHODS

This study selected four types of low-carbon bainitic steel produced by Anyang Iron and Steel Company, and their chemical composition is shown in Table 1. In production, a two-stage controlled rolling process is used, which includes rolling in the austenite recrystallization zone and unrecrystallized zone, followed by accelerated cooling and air cooling after reaching the predetermined temperature. The specific production process is shown in Table 2.

The thermal simulation experiments were conducted on a Gleeble-1500D thermal simulation machine. During the experiments, temperature measurements were taken using a thermocouple, and a computer control system was employed to regulate the specimen's heat flux density, thereby controlling its heating and cooling rate. The steel composition employed was that of Eq. 2, as indicated in Table 1, The experimental process is shown in Fig. 1. Following processing, the specimens were longitudinally sectioned through the center, polished, and then etched

using a 4 % alcoholic nitric acid solution. The resulting microstructures were observed using a HITACHI S-4500 SEM microscope. The presence of MA islands was examined using a metallographic microscope, and the volume fraction of MA islands was quantified using the SISC-8 metallographic analysis software. Microhardness measurements were carried out using an FM-300 digital microhardness tester with an indentation force of 1.96 N.

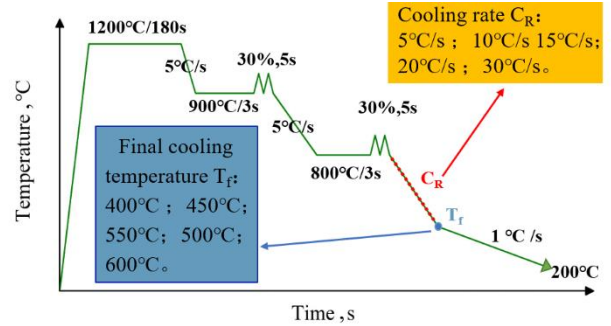


Fig. 1. Schematic diagram of the experimental process

In this experiment, EBSD samples were prepared using ion thinning method. The Gatan Model 600 ion thinning instrument was employed to uniformly remove a thickness of 1 to 20 nm from the sample surface, resulting in a smooth sample surface. SEM samples were prepared using the dual-jet electropolishing method. Disk-shaped samples were loaded into the dual-jet electropolishing instrument, the Struers Tenupol-5, for dual-jet thinning. The electropolishing electrolyte was a 4 % solution of perchloric acid and acetic acid, with an applied voltage of 30 V, current of 30 mA, and a temperature of 243 K. The electropolishing process was conducted for 1.5 minutes in a liquid nitrogen environment to achieve a mirror-like surface. Room temperature tensile tests were conducted on an MTS testing machine, with a strain rate ranging from $2.5 \times 10^{-3}/s$ to $2.5 \times 10^{-4}/s$. The tests were performed according to the GB/T228.1 standard to determine yield strength, tensile strength, and elongation at fracture. Impact tests were conducted following the GB/T 229-199 standard, using V-notch standard samples with dimensions of 10 mm × 10 mm × 55 mm.

Table 1. Chemical composition of test steel, wt. %

Number	Steel grade	Thickness, mm	C	Si	Mn	P	S	Al	Nb	Ti	Cr	Mo	B	V
1	70DB	20	0.055	0.25	1.7	0.01	0.003	0.041	0.054	0.0021	0	0.06	0.0017	0
2	80DB	16	0.064	0.25	1.72	0.014	0.003	0.038	0.054	0.017	0.17	0.117	0.002	0.046
3		20	0.053	0.25	1.75	0.0013	0.001	0.036	0.053	0.017	0.17	0.114	0.0019	0.043
4		25	0.073	0.24	1.68	0.009	0.002	0.022	0.057	0.016	0.18	0.115	0.0017	0.049

Table 2. Typical rolling processes

Number	Steel grade	Thickness, mm	Heating temperature, °C	Heating time, h	Rolling temperature, °C	Second stage rolling temperature, °C	Second stage rolling thickness, mm	Final rolling temperature, °C	Final cooling temperature, °C
1	70DB	20	1250	2.5–3	1090	880	60	790	550
2	80DB	16	1230	2.5–3	1090	940	60	790	460
3		20	1230	2.5–3	1100	920	70	790	460
4		25	1230	2.5–3	1100	900	70	790	460

3. TEST RESULTS AND DISCUSSION

3.1. Continuous transformation curve determination of low carbon bainitic steel

The basic method for studying the transformation behavior of austenite to other phases is to determine the CCT curve by measuring the continuous cooling process of the supercooled austenite in steel. To obtain a bainite structure during the continuous cooling process of low-carbon bainitic steel, it is crucial to inhibit the formation of proeutectoid ferrite, and maintain the stability of austenite until it transforms to bainite below the temperature of Bs. By controlling the cooling rate and final cooling temperature, a bainitic transformation structure can be obtained in low-carbon alloy steel without increasing cost.

In this study, the Mn-Mo-Cr-B series low-carbon bainitic steel was subjected to thermal simulation and combined with metallographic analysis to measure the continuous cooling transformation temperature and curve of deformation-induced austenite. The various transformation temperatures of austenite were determined based on the characteristic points on the curve. The selected cooling rates were 5 °C/s, 10 °C/s, 15 °C/s, 20 °C/s, and 30 °C/s, and the transformation points were determined by the tangent method. The significance of each transformation point was analyzed by metallography, and the experimental phase diagram of the steel is shown in Fig. 2.

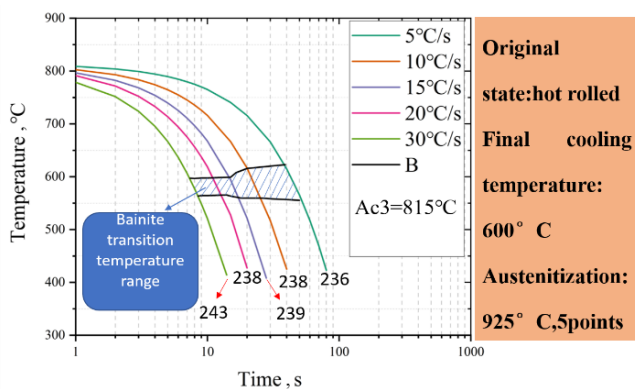


Fig. 2. CCT curve of the test steel

Fig. 2 shows the CCT curve of the tested steel obtained from the thermal simulation test machine. As the cooling rate decreases, the temperature of the bainite transformation increases, and the phase transformation temperature of the tested steel is between 550 °C and 600 °C. Since the primary austenite generally nucleates at the austenite grain boundaries, the added B element strongly segregates to the grain boundaries in the steel, suppressing the nucleation of ferrite. At the same time, niobium has inhibitory effects on the diffusion of carbon and iron atoms, and exerts a drag effect on the migration of phase boundaries, which also suppresses the nucleation and growth of ferrite. Therefore, no ferrite was found in the steel. The tested steel has a low content of austenite stabilizing elements such as C and Mn, and a high transformation temperature, and no martensite was formed as a transformation product. In the cooling rate range studied, the tested steel was all bainite.

3.2. Effect of cooling rate on phase transition

Within the range of bainite transformation, the influence of different cooling rates at the same final cooling temperature (600 °C) on the morphology of bainite structure is shown in Fig. 3. It was observed that the organization of the experimental steel at different cooling rates was mainly composed of bainite with secondary phases, but the proportion of the secondary phase varied with different cooling rates. At a cooling rate of 5 °C/s, the structure was mainly continuous with granular bainite, while at 10 °C/s, the structure was mainly granular bainite with a small amount of lath bainite, and the granular bainite decreased and became finer. When the cooling rate reached 20 °C/s, the structure was mainly composed of lath bainite with a small amount of granular bainite. The lath bainite were distributed between the crossed and chaotic granular bainite, with wider internal laths and non-straight boundaries outlined by residual austenite islands. As the cooling rate increased, the structure gradually shifted from being mainly composed of granular bainite to being mainly composed of lath bainite, and the laths became thinner. The number of MA islands in the bainite increased, and they changed from short rod-shaped or irregular polygons to uniform granules with smaller sizes. This is because, for bainite, the higher the cooling rate, the lower the starting temperature of bainite transformation, the greater the driving force for phase transformation, and the less sufficient carbon diffusion. Therefore, the austenite is only enriched in carbon within a short distance, resulting in a decrease in the size of MA islands, an increase in their number, and a shortened spacing. At the same time, with the increase of cooling rate, the defects in the original austenite increase, resulting in an increase in the nucleation zone of bainitic ferrite and carbon-enriched zone of austenite, which also increases the number of MA islands in the bainite.

3.3. Effect of final cooling temperature on phase transition

The differences in microstructure were observed under SEM and metallography at different final cooling temperatures while using the same cooling rate of 15 °C/s. At a final cooling temperature of 400 °C, the microstructure was mainly composed of lath bainite, with small and finely intersecting lath packets and strong directionality. At 550 °C, the microstructure was a mixed structure of granular bainite and lath bainite, with wider and longer laths and less straight boundaries. As the final cooling temperature increased, the proportion of granular bainite in the microstructure increased, and the laths gradually became wider. At a final cooling temperature of 600 °C, the microstructure was mainly granular bainite. Fig. 4 shows the SEM and metallographic images of the microstructure of the test steel at a final cooling temperature of 400 °C, where the lath features were very distinct. Below 500 °C (400 °C, 450 °C, 500 °C), there was no significant change in the microstructure, and it was mainly composed of lath bainite. Combined with the CCT curve in Fig. 2, it can be seen that the bainite transformation temperature of the test steel was between 550 °C and 600 °C.

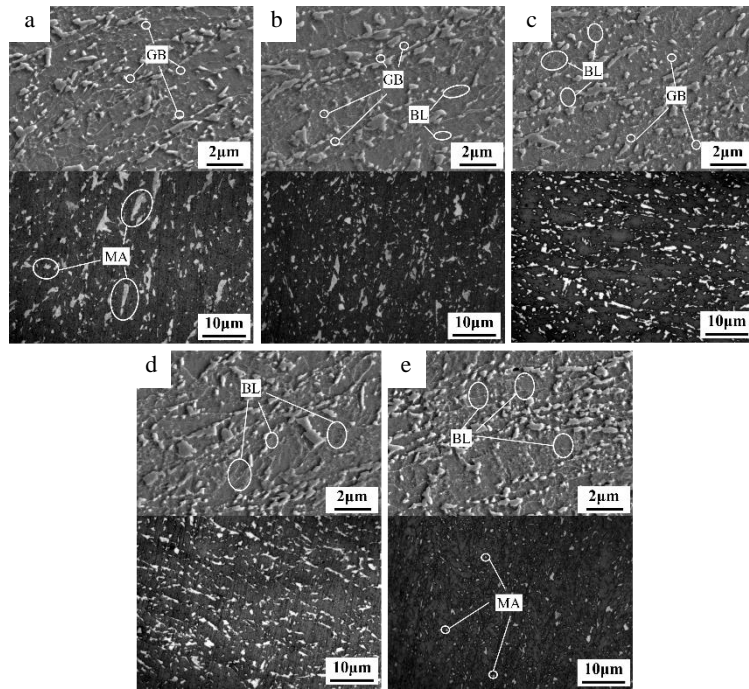


Fig. 3. Microstructure of the test steel at different cooling rates. Cooling rate: a–5 °C/s; b–10 °C/s; c–15 °C/s; d–20 °C/s; e–30 °C/s

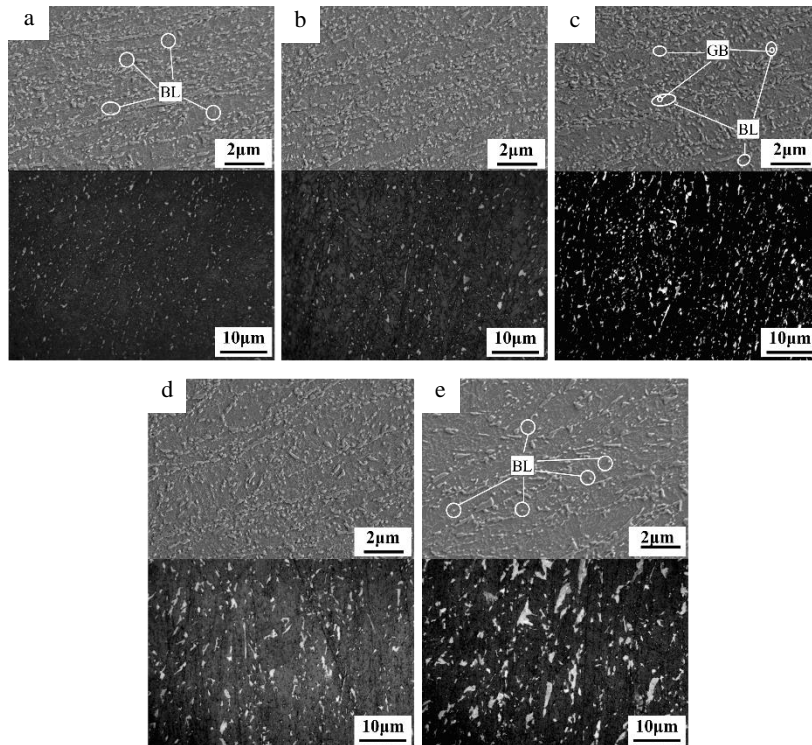


Fig. 4. Microstructure of the test steel at different final cooling temperatures. Final cooling temperature: a–400 °C; b–450 °C; c–500 °C; d–550 °C; e–600 °C

When the final cooling temperature was below 500 °C, this temperature had already reached below the bainite transformation temperature, and the phase transition was completed. All phase transitions occurred during the rapid cooling stage, resulting in a microstructure of lath-shaped bainite. When the final cooling temperature was 600 °C, this temperature entered the bainite transformation temperature zone, and most of the transformation occurred during the slow cooling stage with an actual cooling rate of 1 °C/s. Therefore, the as-rolled microstructure was mainly

composed of bainite and MA constituents, which were larger and distributed between the bainite and martensite-austenite groups. At a final cooling temperature of 550 °C, part of the transformation occurred during the rapid cooling stage, and the remaining transformation occurred during the slow cooling stage.

From the analysis of MA islands in Fig. 4, it can be seen that when the final cooling temperature is low (400 °C), the content of MA islands in the steel is less, accounting for about 4 %, and the particles are uniform and fine, mostly

only 2 ~ 3 μm , and they are dispersed. distribution in the steel, which is very important for bainitic steels to maintain high strength levels while still having good toughness. When the final cooling temperature rises to 500 $^{\circ}\text{C}$, the content of MA islands in the steel increases significantly compared with that at 450 $^{\circ}\text{C}$, reaching 8.7 %, but the particles are still relatively small; with the further increase of the final cooling temperature, there are a large number of sharp-edged islands Blocky MA islands and strip-shaped MA islands appeared. When the final cooling temperature was 600 $^{\circ}\text{C}$, lumpy MA accounted for the majority, and the content of MA islands also increased to 15.9 %.

In order to describe the relationship between MA islands, cooling rate and final cooling temperature more clearly, the volume fraction of MA islands was counted by the particle size analysis method, and plotted in Fig. 5.

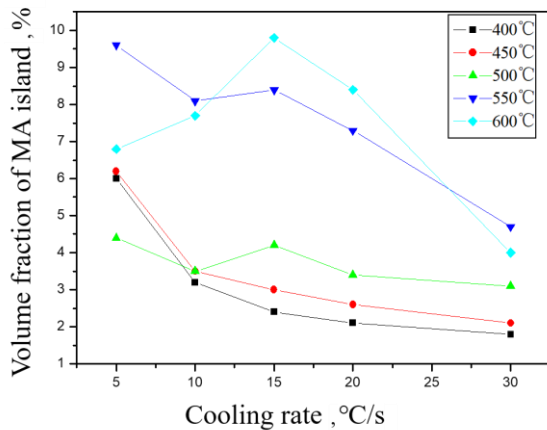


Fig. 5. MA island volume fraction versus cooling rate and final cooling temperature

Combining Fig. 3 and Fig. 5, it can be observed that as the cooling rate increases, the dispersed MA islands become finer and their number increases, but the volume fraction decreases. This is because at higher cooling rates, the start temperature of the bainite transformation is lower, and the diffusion of carbon atoms is insufficient, resulting in the enrichment of carbon within the austenite over a short distance, which in turn leads to a decrease in the size of MA island components within the bainite and an increase in their number. At the same time, the bainite morphology changes from granular to laths, resulting in an increase in dislocation density within the laths. As the final cooling temperature increases, large, chunky and elongated MA islands appear in the steel, leading to a rapid increase in volume fraction.

3.4. Variation law of microhardness during continuous cooling

Microhardness measurements were performed on experimental steel, and the results are shown in Fig. 6. From the figure, it can be seen that below 500 $^{\circ}\text{C}$, the microhardness increases significantly with increasing cooling rate. At 550 $^{\circ}\text{C}$, the microhardness initially increases with increasing cooling rate but then remains constant. At 600 $^{\circ}\text{C}$, the cooling rate has little effect on the hardness. It is believed that the reason for this trend is due to the strengthening of the phase transformation organization. The phase transformation points in the steel

indicate that the starting temperature B_s of the bainite transformation is approximately 600 $^{\circ}\text{C}$, and the ending temperature B_f is approximately 550 $^{\circ}\text{C}$. When the final cooling temperature is around 600 $^{\circ}\text{C}$, all transformations occur during the slow cooling stage, and the main structure formed in the steel is granular bainite with low strength. With an increase in cooling rate and a decrease in the final cooling temperature, the steel structure changes from mainly granular bainite to mainly lath bainite, which rapidly increases the strength of the steel matrix. When the rapid cooling and the final cooling temperature is reduced to the bainite transformation final cooling temperature B_f , the steel organization is mainly fine lath bainite, the tissue strengthening effect is the largest.

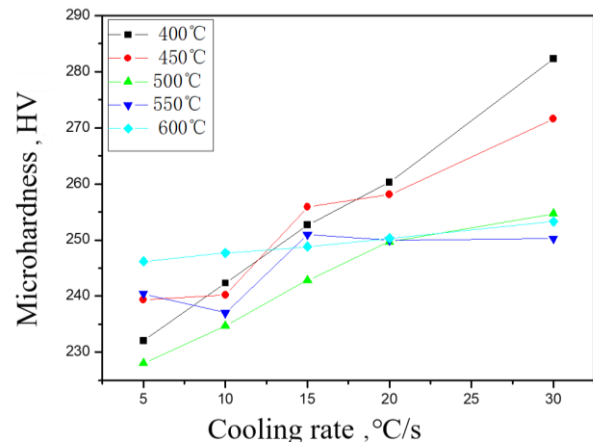


Fig. 6. Microhardness versus cooling rate and final cooling temperature

3.5. Organizational characteristics and crystal orientation analysis of experimental steel

3.5.1. Analysis of organizational characteristics

In sections 3.2 and 3.3, SEM was used to observe the microstructure and phases of steel under different final cooling temperatures and cooling rates. The trends in their changes were analyzed. It was found that there were significant differences in the microstructure and phases of steel under different final cooling temperatures and cooling rates, and the properties of steel depend on its microstructure, which is predominantly determined by phase transformation. In order to investigate the influence of different microstructures on the mechanical properties of steel, four different types of steel with different compositions and cooling processes were analyzed for their microstructures. Predictions of their performance trends were made and verified through mechanical performance testing. The compositions and cooling processes are shown in Table 2 and Table 3.

From the SEM morphology shown in Fig. 7, it is clear that No. 2 steel and No. 3 steel are mainly composed of lath bainite, while No. 1 Steel and No. 4 steel are mainly composed of granular bainite, with a small amount of polygonal ferrite distributed on the bainite matrix. In steels with lath bainite as the main structure, obvious zoning phenomenon can be observed within an original austenite grain, and the boundaries of each zone are clear. Within a bainite region, the lath structures are uniform and parallel to each other, forming a bainite packet.

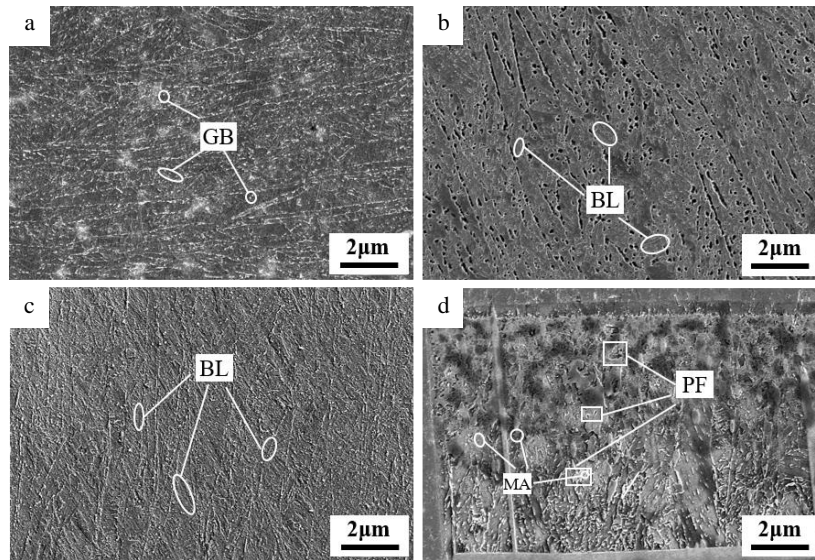


Fig. 7. SEM image of test steel: a–No. 1 steel; b–No. 2 steel; c–No. 3 steel; d–No. 4 steel

The width of a bainite plate is between 0.7–1.2 μm , and its length is between 6–9 μm . There are some polygonal ferrites with a fraction of about 20 % distributed within the original austenite grain. In steels with granular bainite as the main structure, many band-like bainite structures are distributed along the rolling direction within austenite grains, with no directional distribution and unclear boundaries. This can easily be confused with the boundaries of lath bainite in optical microstructures [20]. About 5 %–10 % polygonal ferrites and a small amount of lath bainite are distributed on the granular bainite matrix. Both types of steel, whether composed mainly of granular or lath bainite, have a certain amount of blocky polygonal ferrite distributed along the grain boundaries. These appear as bright white in the microscope, with clear boundaries and a certain contrast with the surrounding bainite, presenting an irregular height and shape, and occasionally MA islands can be seen on the polygonal ferrite matrix.

3.5.2 Analysis of crystal orientation

The EBSD testing system is used to characterize the crystallographic features of the test steel in order to study the distribution of crystal orientations and different angle grain boundaries.

Fig. 8 shows the orientation maps and orientation deviation angle ratio distribution maps of different experimental steels obtained by the EBSD testing system. The colors in the orientation maps represent crystallographic orientation, and grain boundaries are distinguished by their sizes of angles with a boundary angle of 10° . The vertical axis represents relative frequency, and the horizontal axis represents the grain orientation deviation angle. Taking the example of No. 2 Steel in Fig. 8 d, the region enclosed by the black line represents the bainite structure with orientation deviation angles less than 10° , and it can be observed that:

1. There are several large-angle grain boundaries within a lath packet, and adjacent lath blocks are connected by small-angle grain boundaries. The boundary angle between lath blocks is approximately 60° , which is the same as the orientation deviation angle of large-angle

grain boundaries or lath block boundaries, and there is a twinning relationship between lath blocks [21].

2. Different orientations can be observed within bainite lath packets, indicating that there are smaller substructures with larger orientation deviation angles within the lath packets. Therefore, a lath packet can be divided into several parallel regions, called lath blocks [22]. Marder [23] believed that a lath block is a collection of bainitic laths with the same crystallographic orientation, and the lath block boundary is a large-angle grain boundary, while small-angle grain boundaries exist within the lath block.
3. The region enclosed by the black line represents an original austenite grain, and there are four types of lath packets within an original austenite grain. Fig. 8 represents one type of lath packet, and each lath packet contains six lath blocks, and they are six of V1, V2, V3, V4, V5, V6. There are specific combinations between the six variables: V1 and V4, V2 and V5, V3 and V6, which represent three different orientations, and colors that are similar represent the same orientation. In any phase transformation, especially in non-diffusion phase transformations, nucleation and growth must follow the principle of minimizing interfacial energy and volumetric strain energy [24, 25].

The specific combinations between the six variables exist because during the formation and growth of bainitic nuclei, there are two types of interfaces: one is the interface between the parent austenite phase and the bainite phase, which follows the Kurdjumov-Sachs or Nishiyama-Wassermann relationships and can achieve the minimum interfacial energy and volumetric strain energy [26, 27]. The other type of interface is the interface between adjacent bainite single crystals, and the principle is that the interfacial energy and volumetric strain energy between adjacent bainitic single crystals should be as low as possible [28]. Therefore, there are only two types of internal boundaries in bainite structures: small-angle boundaries and twinned boundaries. Therefore, the six variables within a lath block are combined in a specific way to achieve the minimum interfacial energy and volumetric strain energy.

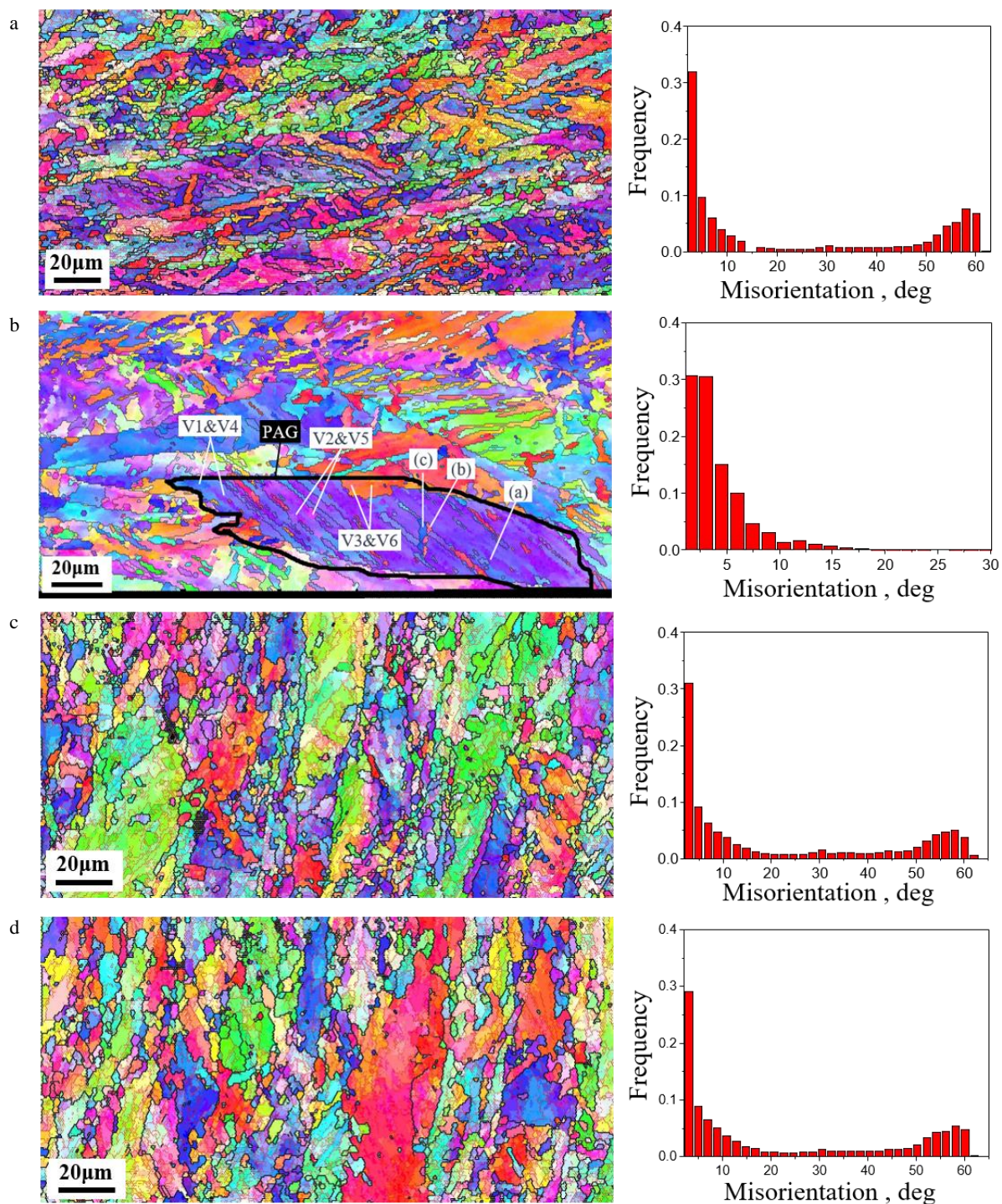


Fig. 8. Grain boundary orientation diagram of steel and corresponding grain boundary orientation difference distribution plot: a–No. 1 steel; b–No. 2 steel; c–No. 3 steel; d–No. 4 steel

Fig. 9 is a schematic diagram of bainite laths. It can be seen from the figure that the austenite grains are composed of several lath packets, and the lath packets are divided into several parallel regions as lath blocks. The length of the lath blocks in the direction is parallel to the lath boundary, and there is a high-angle grain boundary between the laths. The lath block is composed of several laths, and each lath is a single crystal. The width of the slats with large grain size is relatively uniform, while one slat in the lath packet with small grain size dominates, and the other slats are very small.

3.6. The effect of crystal orientation on steel properties

According to the theory of grain boundary design and control, the proportions of small angle and large angle grain boundaries are different, and there are differences in material toughness. The higher the proportion of small angle grain boundaries, the higher the Charpy plateau [29]. Compared to large angle grain boundaries, small angle grain boundaries have superior properties of inactivity and crack resistance [30].

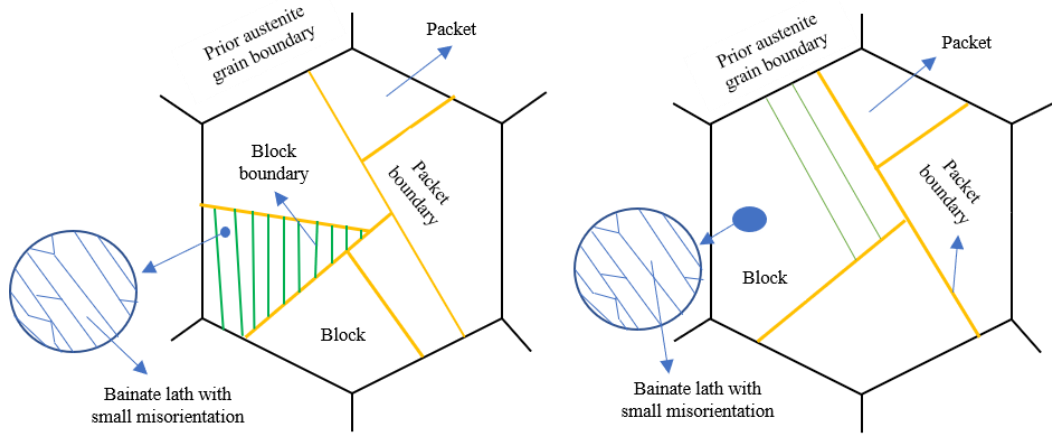


Fig. 9. Schematic diagram of bainite slats: a – large grain size; b – small grain size

An increase in the ratio of small angle grain boundaries and the dispersion of M-A islands can improve resistance to crack propagation [31, 32]. In other words, the smaller the size of the lath block and lath packet, the higher the proportion of small angle grain boundaries, and the better the resistance and toughness against cracking.

Research by M. Pontremoli et al. [33] has demonstrated that the grain size of a tissue associated with the same lattice orientation controls the macroscopic mechanical properties (such as strength and toughness). Analysis suggests that when a crack encounters a high-energy large angle grain boundary, it will quickly propagate, causing the material to fracture along a brittle grain boundary. However, when a crack encounters a low-energy small angle grain boundary, the propagation will be inhibited or changed to transgranular fracture, thereby improving the material toughness.

3.7. Mechanical properties of test steel test results

Verify the influence of the microstructure and crystal orientation on the strength and toughness of steel by conducting mechanical performance testing on the steel.

3.7.1. Mechanical performance test results

Mechanical property tests were conducted on steel plates with the same composition, rolling, and cooling conditions, and the specific results are analyzed below. From Fig. 10, it can be seen that the elongation of 80DB grade steel plates has already reached the target requirement ($\geq 14\%$), while the yield strength has not yet fully reached the target (≥ 690 MPa).

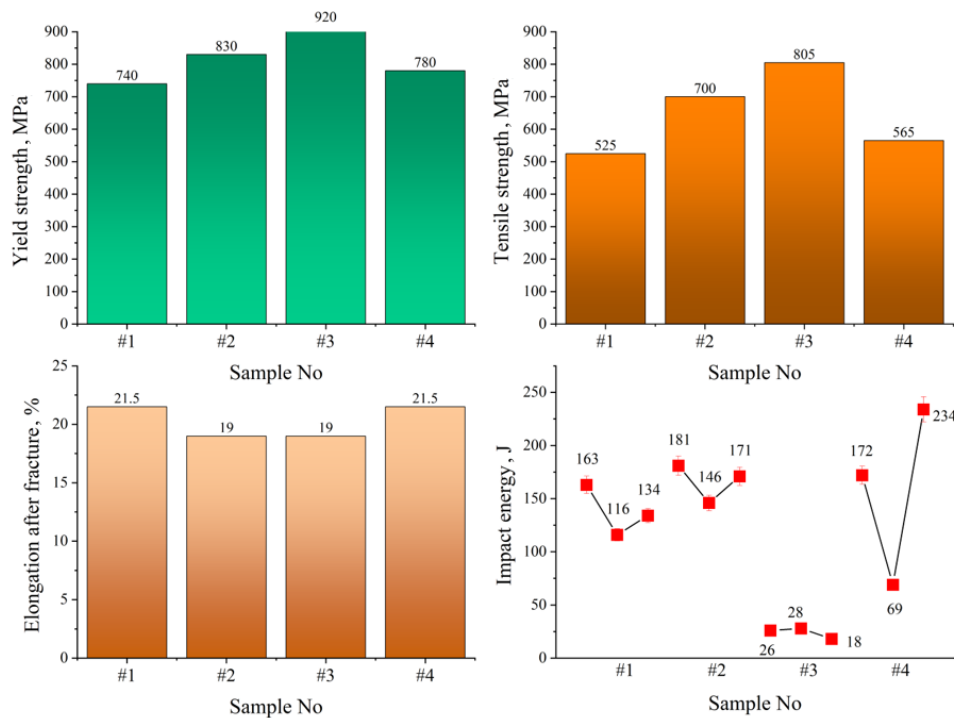


Fig. 10. Basic mechanical properties of the test steel

By analyzing the bainitic microstructure distribution shown in Fig. 7 and the mechanical properties presented in Fig. 10, it is observed that the steel with a lath-like bainitic structure exhibits higher strength compared to the steel with a granular bainitic structure.

Furthermore, as the lath-like structure becomes finer, the increase in strength becomes more pronounced. However, this enhanced strength is accompanied by reduced ductility, and the microstructure has minimal impact on toughness.

3.7.2. Micromorphological analysis of test samples

SEM morphology of the tensile fracture surface of low carbon bainitic steel at room temperature is shown in Fig. 11. It can be observed from the figure that the fracture is ductile and exhibits a dimple morphology. As the yield strength decreases, the size and depth of the dimples become smaller and shallower. Conversely, with an increase in yield strength, the size and depth of the dimples begin to increase.

Careful observation of the fracture surface of ductile fracture reveals in every pit, there are inclusions or their traces. This indicates that the formation of these pits, known as dimples, is related to second-phase particles [34]. Extensive plastic deformation results in the formation of a large number of different-oriented dislocation loops around the second-phase particles, and the cross-section perpendicular to the dislocation loops is a dislocation pile-up group [35]. Under stress, serious stress concentration occurs at the top of the pile-up group.

As the external force increases and the number of dislocations in the pile-up group increases, the stress

concentration at the top of the pile-up group increases. When it reaches a certain level, the second-phase separates from the matrix, creating a new surface. The large number of dislocations released at the top of the pile-up group cause new interfaces to form, and each dislocation released increases the size of the interface. The release of a large number of dislocations in all directions causes the complete separation of the second phase from the matrix in the direction of maximum shear force, and the micropores in this direction continue to expand during further deformation. Between the two adjacent micropores, the matrix material undergoes uniform deformation under external forces, and the diameter decreases. When the matrix material between the two adjacent micropores is pulled apart, the micropores connect with each other and fracture occurs.

Fig. 12 shows the metallographic, SEM, and TEM images with different yield strengths. From the images, it can be observed that there are differences in the microstructure of materials with different yield strengths. Specifically, for the sample with a yield strength of 525 MPa, the microstructure mainly consists of granular bainite and quasi-polygonal ferrite. In the SEM image, residual austenite forming MA islands inside the granular bainite has a larger size and less frequent occurrence with no regular distribution. When the yield strength reaches 565 MPa, the microstructure still consists of granular bainite and quasi-polygonal ferrite, but the granular bainite becomes smaller with an increase in the number of MA islands and a decrease in their size.

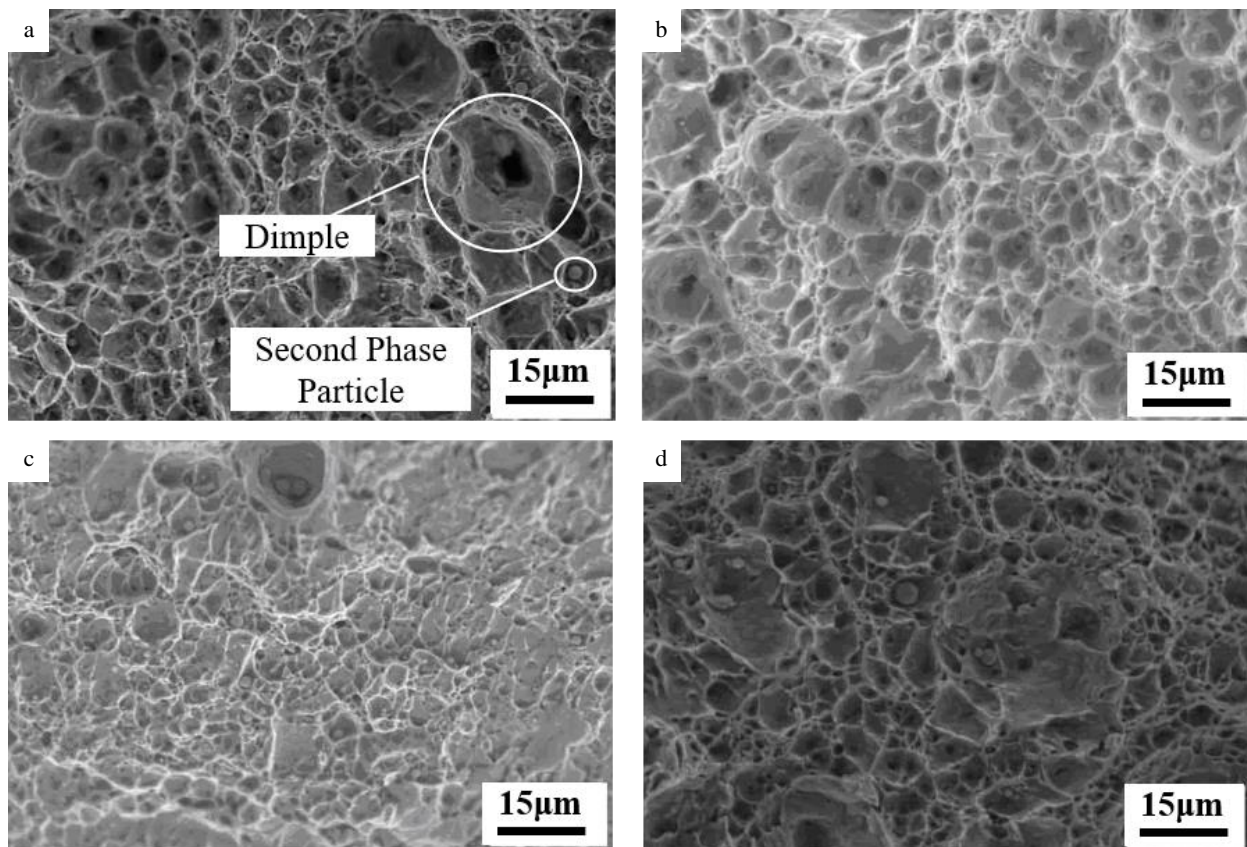


Fig. 11. Tensile fracture profile of the test steel at room temperature. Yield strength: a – 525 MPa; b – 565 MPa; c – 700 MPa; d – 805 MPa

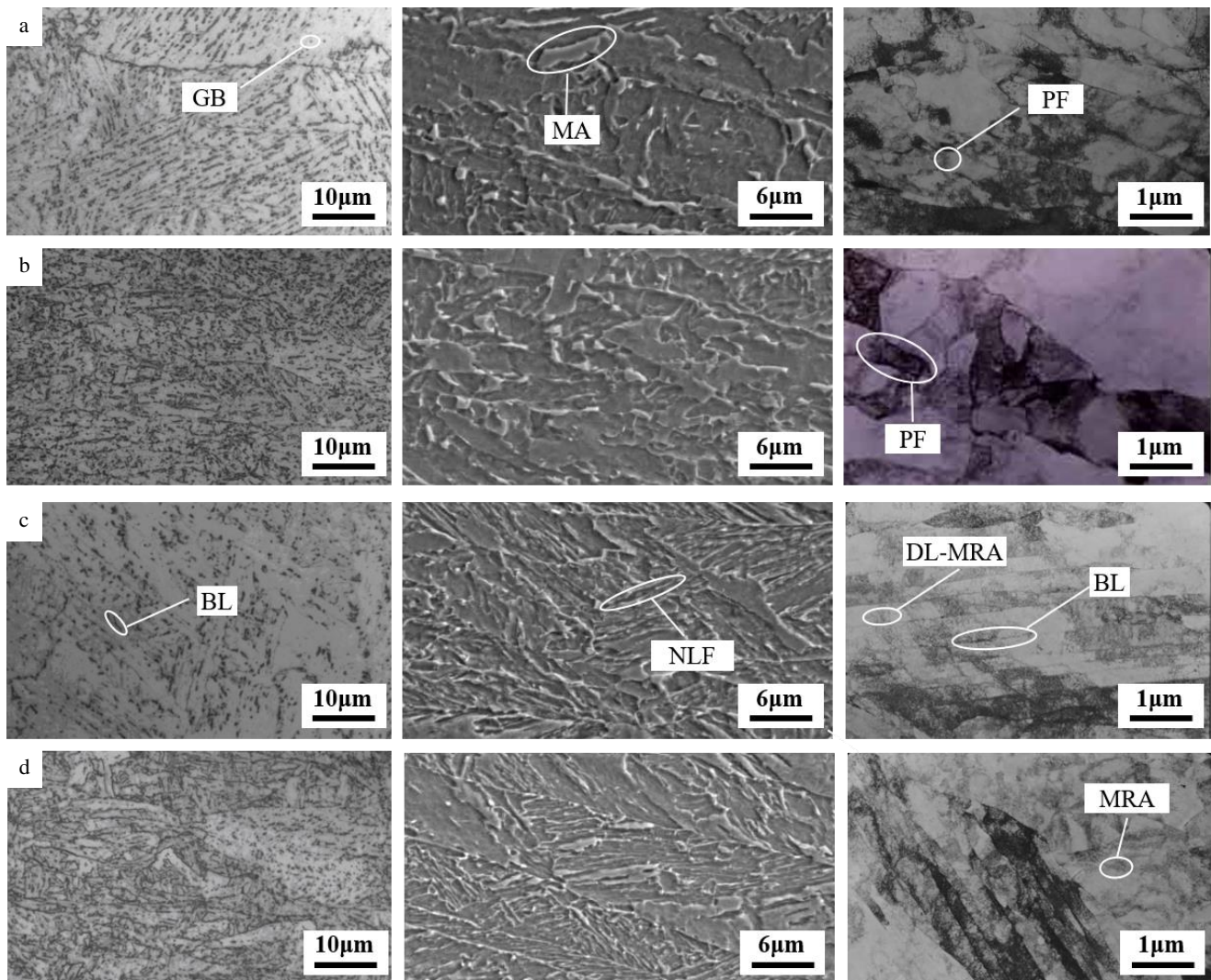


Fig. 12. Metallographic, SEM and TEM diagrams of test steel. Yield strength: a – 525 MPa; b – 565 MPa; c – 700 MPa; d – 805 MPa

When the yield strength reaches 700 MPa, the proportion of lath bainite in the microstructure becomes dominant, while the granular bainite decreases and there is a certain amount of acicular ferrite. In this microstructure, the original austenite grain boundaries are obvious, and the granular bainite appears irregularly elongated (or in a few cases, block-shaped), mainly forming along the grain boundaries. There are more lath bainite and wider laths in the steel, with discontinuous residual austenite in between the laths. The number of acicular ferrite within the grains is significant, and they cross each other, dividing the bainite lath packets. Fig. 12 d shows the microstructure of the sample with a yield strength of 805 MPa, which is mainly composed of lath bainite with straight boundaries and strong directionality. The original granular bainite remains unchanged, and the residual austenite MA islands become dispersed and small.

4. CONCLUSIONS

The following conclusions are drawn in this article:

1. Under a cooling rate of 5°C/s, a granular bainitic structure is formed. With an increase in the cooling rate, the lath-like bainitic structure gradually becomes more

prevalent and the laths become finer. The dispersion and size of the martensite islands become more pronounced. The bainite transformation temperature for the test steel lies between 550 °C and 600 °C. When the final cooling temperature is below 500 °C, the as-rolled structure is primarily composed of lath-like bainite. As the final cooling temperature increases, the structure gradually transforms into granular bainite, and the laths become wider and longer while the martensite island size increases. With an increase in the cooling rate, the microhardness increases; however, the microhardness decreases with a rise in the final cooling temperature. This decrease is especially significant at lower final cooling temperatures, and there is almost no change at 600 °C.

2. In the test steel, the microstructure of bainite consists of primary austenite grains, laths packet, and lath blocks in sequence. Observations reveal that the substructure within the laths packet of bainite consists of lath blocks with different orientations. As the size of the lath blocks and bundles increases, the material's strength decreases. In other words, the presence of longer and wider laths packet in the steel is a key factor influencing its strength.

3. Steels with a lath-like bainitic structure exhibit higher strength compared to those with a granular bainitic structure. The finer the laths, the more significant the strength enhancement, although this comes at the cost of reduced ductility. It's worth noting that the microstructural effect on toughness is relatively minor. Through the aforementioned research, preliminary insights have been gained into the reasons behind the reduced impact toughness in this type of low carbon bainitic steel. In practical production, effective enhancement of the mechanical properties of such steels can be achieved by controlling the cooling process, improving steel cleanliness, minimizing inclusions, and managing the size of primary austenite grains, particularly the laths packet.

REFERENCES

- Kumnorkaew, T., Lian, J., Uthaisangasuk, V., Zhang, J., Bleck, W.** Low Carbon Bainitic Steel Processed by Ausforming: Heterogeneous Microstructure and Mechanical Properties *Materials Characterization* 194 2022: pp.112466
<https://doi.org/10.1016/j.matchar.2022.112466>
- Wang, S.C., Kao, P.W.** The Effect of Alloying Elements on The Structure and Mechanical Properties of Ultra Low Carbon Bainitic Steels *Journal of Materials Science* 28 1993: pp. 5169–5175.
<https://doi.org/10.1007/BF00570058>
- Feng, C., Bai, B.Z., Zheng, Y.K.** Effect of 0.06% Nb on the Microstructure and Mechanical Properties of Mn-Series Low Carbon Air-Cooling Bainitic Steels *Advanced Materials Research* 284 2011: pp. 1191–1195.
<https://doi.org/10.4028/www.scientific.net/AMR.284-286.1191>
- Senthil, P.P., Rao, K.S., Nandi, H.K., Singh, V., Kumar, S., Sankaran, S., Kumar, K.S., Madhu, V.** Influence of Niobium Microalloying on the Microstructure and Mechanical Properties of High Carbon Nano Bainitic Steel *Procedia Structural Integrity* 14 2019: pp. 729–737.
<https://doi.org/10.1016/j.prostr.2019.05.091>
- Garmeh, B., Kasiri, A.M., Amini, K., Ghayou, H., Bakhsheshi, R.H.R., Berto, F.J.A. S.** Effect of Vanadium and Rare Earth on the Structure, Phase Transformation Kinetics and Mechanical Properties of Carbide-Free Bainitic Steel Containing Silicon *Applied Sciences* 12 (3) 2022: pp. 1668.
<https://doi.org/10.3390/APP12031668>
- Zhu, W., Cui, J., Feng, Y., Chen, Z., Zhao, Y., Chen, L.** Achieving Excellent Strength-Ductility Balance and Lower Yield Ratio in a 690 Mpa-Grade Multiphase Construction Steel *Steel Research International* 93 (7) 2022: pp. 2100750.
<https://doi.org/10.1002/SRIN.202100750>
- He, B.B., Xu, W., Huang, M.** Effect of Boron on Bainitic Transformation Kinetics After Ausforming in Low Carbon Steels *Journal of Materials Science Technology* 33 (12) 2017: pp. 1494–1503.
<https://doi.org/10.1016/j.jmst.2017.05.006>
- Lan, L.Y., Chang, Z.Y., Fan, P.H.** Exploring the Difference in Bainite Transformation with Varying the Prior Austenite Grain Size in Low Carbon Steel *Metals* 8 (12) 2018: pp. 988.
<https://doi.org/10.3390/met8120988>
- Long, X.Y., Sun, D.Y., Wang, K., Zhang, F.C., Yang, Z., Li, Y., Zheng, C.** Effect of Carbon Distribution Range in Mixed Bainite/Martensite/Retained Austenite Microstructure on Mechanical Properties *Journal of Materials Research Technology* 17 2022: pp. 898–912.
<https://doi.org/10.1016/J.JMRT.2021.12.121>
- Garcia, C.I., Lis, A., Pytel, S., Deardo, A.** Ultra-Low Carbon Bainitic Plate Steels: Processing, Microstructure and Properties *Iron & Steelmaker* 13 (3) 1991: pp. 103–112.
- Wang, H., Yang, L.** Effect of Different Welding Energy on Microstructure and Toughness of HAZ of Low Carbon Bainitic Steel *International Journal of Modern Physics B* 34 (32) 2020: pp. 2050319.
<https://doi.org/10.1142/S0217979220503191>
- Yang, L., Wang, H.** Orthogonal Optimum Design of Parameters of Flux Used for Low Carbon Bainitic Steel *Applied Physics A* 126 (7) 2020: pp. 538.
<https://doi.org/10.1007/s00339-020-03730-z>
- Chen, D., Wang, Z., Zhang, Y., Lian, H., Shang, Y., Fan, M., Dai, L., Sun, L., Cui, Y., Zhang, Z.** Effects of Thermo-Mechanical Treatments on the Microstructure and Mechanical Properties of a 460 Mpa Grade Low Carbon Bainitic Ferrite Steel *Materials Science Engineering: A* 842 2022: pp. 143087.
<https://doi.org/10.1016/J.MSEA.2022.143087>
- Xi, G.G., Ma, Q.** The Research Situation and Development Prospect of Bainitic Steels *Materials Reports* 20 (2) 2006: pp. 78–81.
- Yang, Z.N., Zhang, F.H., Zheng, C.L., Zhang, M., Lv, B.** Study on Hot Deformation Behaviour and Processing Maps of Low Carbon Bainitic Steel *Materials Design* 66 2015: pp. 258–266.
<https://doi.org/10.1016/j.matdes.2014.10.068>
- Zhou, Q., Qian, L.H., Meng, J.Y., Zhao, L.J.** The Fatigue Properties, Microstructural Evolution and Crack Behaviors of Low-Carbon Carbide-Free Bainitic Steel During Low-Cycle Fatigue *Materials Science Engineering: A* 820 2021: pp. 141571.
<https://doi.org/10.1016/j.msea.2021.141571>
- Yang, X., Yu, W., Tang, D., Chen, Z., Fan, J., Shi, J., Wang, L., Sun, D.** Effect of Air Cooling Time on Temperature and Microstructure Uniformity of 960 Mpa High Strength Steel by Direct Quenching *Materialwissenschaft Und Werkstofftechnik* 53 (11) 2022: pp. 1347–1356.
<https://doi.org/10.1002/MAWE.202100267>
- Nikolai, K.** Cooling Process Optimization During Hardening Steel in Water Polyalkylene Glycol Solutions *Technology Audit and Production Reserves* 6 (1) 2021: pp. 27–35.
<https://doi.org/10.15587/2706-5448.2021.247736>
- Robert, T., John, W.** Identifying and Quantifying Energy Savings on Fired Plant Using Low Cost Modelling Techniques *Applied Energy* 89 (1) 2012: pp. 127–132.
<https://doi.org/10.1016/j.apenergy.2011.01.061>
- Sitzman, S.D.** Introduction to EBSD Analysis of Micro-to Nanoscale Microstructures in Metals and Ceramics *Testing, Reliability, and Application of Micro- and Nano-Material Systems II* 5392 2004: pp. 78–90.
<https://doi.org/10.1117/12.542082>
- Hwang, B., Kim, Y.G., Lee, S., Kim, Y.M., Kim, N.J., Yoo, J.Y.** Effective Grain Size and Charpy Impact Properties of High-Toughness X70 Pipeline Steels *Metallurgical Materials Transactions A* 36 (8) 2005: pp. 2107–2114.
<https://doi.org/10.1007/s11661-005-0331-9>
- Huang, X.X., Tsuzaki, K., Maki, T.** Subgrain Growth and Misorientation of the A Matrix in an (A+ Γ) Microduplex Stainless Steel *Acta Metallurgica Et Materialia* 43 (9) 1995: pp. 3375–3384.

- [https://doi.org/10.1016/0956-7151\(95\)00028-T](https://doi.org/10.1016/0956-7151(95)00028-T)
23. **Kim, M.C., Oh, Y.J., Hong, J.H.** Characterization of Boundaries and Determination of Effective Grain Size in Mn-Mo-Ni Low Alloy Steel From the View of Misorientation *Scripta Materialia* 43 (5) 2000: pp. 205–211. [https://doi.org/10.1016/S1359-6462\(00\)00392-4](https://doi.org/10.1016/S1359-6462(00)00392-4)
 24. **Koyama, M., Saitoh, H., Sato, T., Orimo, S.I., Akiyama, E.** Hydrogenation Treatment Under Several Gigapascals Assists Diffusionless Transformation in a Face-Centered Cubic Steel *Scientific Reports* 11 (1) 2021: pp. 19384. <https://doi.org/10.1038/S41598-021-98938-1>
 25. **Liu, J., Liu, W.Z., Guan, B., Wang, B., Shi, L., Jin, F., Zheng, Z.G., Wang, J.X., Ikeda, T.M., Jiang, L.** Diffusionless Transformation of Soft Cubic Superstructure From Amorphous to Simple Cubic and Body-Centered Cubic Phases *Nature Communications* 12 (1) 2021: pp. 3477. <https://doi.org/10.1038/S41467-021-23631-W>
 26. **He, Y.S., Gao, J.B., He, Y.Z., Shin, K.** A New Fcc-Bcc Orientation Relationship Observed in the Strain-Induced Martensitic Transformation of an Austenitic Stainless Steel *Materials Letters* 305 2021: pp. 130735. <https://doi.org/10.1016/J.MATLET.2021.130735>
 27. **Köse, C., Topal, C.** Dissimilar Laser Beam Welding of AISI 2507 Super Duplex Stainless to AISI 317L Austenitic Stainless Steel *Materials Science Engineering: A* 862 2023: pp. 144476. <https://doi.org/10.1016/J.MSEA.2022.144476>
 28. **Lin, G.** Carbon-Based Micro/Nano Devices For Transistors, Sensors, and Memories *Journal of Physics: Conference Series* 2152 2021: pp. 257–268. <https://doi.org/10.1088/1742-6596/2152/1/012033>
 29. **Yu, H.** Influences of Microstructure and Texture on Crack Propagation Path of X70 Acicular Ferrite Pipeline Steel *Journal of University of Science Technology Beijing, Mineral, Metallurgy, Material* 15 (6) 2008: pp. 683–687. [https://doi.org/10.1016/S1005-8850\(08\)60271-6](https://doi.org/10.1016/S1005-8850(08)60271-6)
 30. **Xi, X.H., Wang, J.L., Chen, L.Q., Wang, Z.D.** Tailoring Mechanical Properties of a Low Carbon Cu-Containing Structural Steel by Two-Step Intercritical Heat Treatment *Metals Materials International* 25 (6) 2019: pp. 1477–1487. <https://doi.org/10.1007/s12540-019-00343-x>
 31. **Lan, L.Y., Qiu, C.L., Song, H.Y., Zhao, D.W.** Correlation of Martensite–Austenite Constituent and Cleavage Crack Initiation in Welding Heat Affected Zone of Low Carbon Bainitic Steel *Materials Letters* 125 2014: pp. 86–88. <https://doi.org/10.1016/j.matlet.2014.03.123>
 32. **Mao, G.J., Cayron, C., Cao, R., LogÉ, R., Chen, J.H.** The Relationship Between Low-Temperature Toughness and Secondary Crack in Low-Carbon Bainitic Weld Metals *Materials Characterization* 145 2018: pp. 516–526. <https://doi.org/10.1016/j.matchar.2018.09.012>
 33. **Pontremoli, M.** Metallurgical and Technological Challenges for the Development of High-Performance X100-X120 Linepipe Steels *Proceeding of the Second International Conference on Advanced Structural Steels (ICASS 2004), Shanghai, China* 39 2004: pp. 57–63.
 34. **Sakasegawa, H., Hirose, T., Kohyama, A., Katoh, Y., Harada, T., Asakura, K., Kumagai, T.** Effects of Precipitation Morphology on Toughness of Reduced Activation Ferritic/Martensitic Steels *Journal of Nuclear Materials* 307 (1) 2002: pp. 490–494. [https://doi.org/10.1016/S0022-3115\(02\)01083-8](https://doi.org/10.1016/S0022-3115(02)01083-8)
 35. **Zhao, L.Y., Wang, Q.F., Shi, G.H., Yang, X.Y., Qiao, M.L., Wu, J.P., Zhang, F.C.** In-Depth Understanding of the Relationship Between Dislocation Substructure and Tensile Properties in a Low-Carbon Microalloyed Steel *Materials Science Engineering: A* 854 2022: pp. 143681. <https://doi.org/10.1016/J.MSEA.2022.143681>



© Cao et al. 2023 Open Access This article is distributed under the terms of the Creative Commons Attribution 4.0 International License (<http://creativecommons.org/licenses/by/4.0/>), which permits unrestricted use, distribution, and reproduction in any medium, provided you give appropriate credit to the original author(s) and the source, provide a link to the Creative Commons license, and indicate if changes were made.